H I-SELECTED GALAXIES IN THE SLOAN DIGITAL SKY SURVEY. I. OPTICAL DATA

The Astronomical Journal, 139:315–328, 2010 February doi:10.1088/0004-6256/139/2/315

H I-SELECTED GALAXIES IN THE SLOAN DIGITAL SKY SURVEY. I. OPTICAL DATA

Andrew A. West[1,2,3,4], Diego A. Garcia-Appadoo[5,6], Julianne J. Dalcanton[2], Mike J. Disney[6], Constance M. Rockosi[7], Željko Ivezić[2], Misty C. Bentz[2,8], and J. Brinkmann[9]

[1] Department of Astronomy, University of Washington, Box 351580, Seattle, WA 98195, USA; aawest@bu.edu
[2] Astronomy Department, 601 Campbell Hall, University of California, Berkeley, CA 94720-3411, USA
[3] MIT Kavli Institute for Astrophysics and Space Research, 77 Massachusetts Ave, 37-582c, Cambridge, MA 02139-4307, USA
[4] Department of Astronomy, Boston University, 725 Commonwealth Ave, Boston, MA 02215, USA
[5] European Southern Observatory, Alonso de Cordova 3107, Casilla 19001, Vitacura, Santiago 19, Chile
[6] Cardiff School of Physics and Astronomy, Cardiff University, Queens Buildings, The Parade, Cardiff, CF24 3AA, UK
[7] UCO/Lick Observatory, Department of Astronomy and Astrophysics, University of California, Santa Cruz, CA 95064, USA
[8] Department of Physics and Astronomy, 4129 Frederick Reines Hall, University of California, Irvine, CA 92697-4575, USA
[9] Apache Point Observatory, P.O. Box 59, Sunspot, NM 88349, USA

Received 2006 November 30; accepted 2009 October 11; published 2009 December 16

ABSTRACT

We present the optical data for 195 H I-selected galaxies that fall within both the Sloan Digital Sky Survey (SDSS) and the Parkes Equatorial Survey (ES). The photometric quantities have been independently recomputed for our sample using a new photometric pipeline optimized for large galaxies, thus correcting for SDSS's limited reliability for automatic photometry of angularly large or low surface brightness (LSB) galaxies. We outline the magnitude of the uncertainty in the SDSS catalog-level photometry and derive a quantitative method for correcting the over-sky subtraction in the SDSS photometric pipeline. The main thrust of this paper is to present the ES/SDSS sample and discuss the methods behind the improved photometry, which will be used in future scientific analysis. We present the overall optical properties of the sample and briefly compare to a volume-limited, optically selected sample. Compared to the optically selected SDSS sample (in the similar volume), H I-selected galaxies are bluer and more luminous (fewer dwarf ellipticals and more star formation). However, compared to typical SDSS galaxy studies, which have their own selection effect, our sample is bluer, fainter, and less massive.

Key words: galaxies: evolution – galaxies: fundamental parameters – galaxies: general – galaxies: photometry – radio lines: galaxies – surveys

Online-only material: color figure, machine-readable and VO tables

1. INTRODUCTION

Galaxies in the local universe span a range of star formation histories. At the beginning of the spectrum are gas-rich, low surface brightness (LSB) galaxies that either have just begun the process of star formation or have been processing their gas with extremely low efficiencies. At the other end are gas-poor galaxies that typically have formed the bulk of their stars in the distant past and are currently devoid of gas (Roberts 1963; McGaugh & de Blok 1997).

Creating a sample that bridges these two regimes requires the union of two different methods of identifying galaxies. Stars dominate the visible light output of most galaxies, and thus galaxies detected by traditional optical imaging have well-developed stellar populations. In contrast, the natural way to identify gas-rich, less evolved galaxies is by their 21 cm radio emission. Selecting on H I reveals galaxies entirely based on their gas content, independent of their starlight, and thus easily finds systems with intact gas reservoirs (e.g., Rosenberg & Schneider 2000). Characterizing the stellar and gaseous properties of galaxies selected in the radio and in the optical will therefore yield information about the entire continuum of galaxy star formation histories (Burkholder et al. 2001).

Aside from its importance for global star formation, a sample of gaseous and stellar information for galaxies in the nearby universe also allows for a more complete census of the local baryons (Rosenberg et al. 2005). Too often, galaxy studies neglect the fact that H I dominates the baryonic content of many galaxies, particularly those with low masses. The baryonic makeup of the nearby universe puts important observational constraints on simulations of galaxy formation and evolution as well as revealing reservoirs of mass that were previously undetected because of their optical LSB nature (Disney 1976). The H I data also provide kinematic constraints on the dark matter content of the galaxies (Blanton et al. 2008). Therefore, with both optical and H I information, we can probe how the baryonic content relates to total mass of the galaxy.

We present the first step toward an inventory of the H I and optical properties of nearby galaxies. Our study focuses on an H I-selected sample and therefore identifies many systems that have retained much of their primordial H I. It lacks the systems that have used their entire gas supply and are dominated by stars. A separate project is underway to complete the nearby baryonic census by filling in the gas-poor systems with H I observations of optically selected galaxies.

This study combines data from two high-quality, uniform surveys, the Parkes Equatorial Survey (ES; Garcia-Appadoo et al. 2009) and the Sloan Digital Sky Survey (SDSS; York et al. 2000; Gunn et al. 1998; Fukugita et al. 1996; Hogg et al. 2001; Smith et al. 2002; Stoughton et al. 2002; Pier et al. 2003; Ivezić et al. 2004; Gunn et al. 2006; Tucker et al. 2006). The combination of these two surveys creates a rich compendium of stellar and H I parameters for galaxies at various evolutionary states that will be used in future papers to explore how global star formation proceeds in galaxies as a function of their physical parameters.

Previously, most H I surveys were targeted at specific locations; thus, little was known about the distribution of H I

in the universe, independent of optical properties. Henning (1992, 1995) used the NRAO 300 ft telescope to conduct an H I blind survey and recovered 39 sources. Large blind surveys followed using the Arecibo 300 m telescope, yielding hundreds of sources and allowing for the first statistically sound studies of the H I mass function (Zwaan et al. 1997; Spitzak & Schneider 1998; Rosenberg & Schneider 2000; Rosenberg & Schneider 2002). These blind surveys also identified many un-cataloged LSB galaxies and paved the way for more complete studies of the baryonic content of nearby galaxies (Rosenberg et al. 2005).

Recent studies have combined large H I surveys with optical and infrared samples, namely the Arecibo Duel Beam and Slice Surveys with the Two Micron All Sky Survey (2MASS; Jarrett et al. 2000; Rosenberg et al. 2005), the merging of the H I Parkes All Sky Survey (HIPASS) with SuperCOSMOS (Hambly et al. 2001a, 2001b, 2001c; Doyle et al. 2005), and the combination of HIPASS with DSS/POSSII data (Wong et al. 2009). Rosenberg et al. (2005) were able to probe the baryonic content of a large sample of galaxies, but were limited by the shallow depth of 2MASS, which does not have data for many of the LSB galaxies in the sample. The HIPASS/SuperCOSMOS/DSS samples of Doyle et al. (2005) and Wong et al. (2009) contain optical/IR data for several thousand H I-selected galaxies but also suffer from the shallow depth of the SuperCOSMOS/DSS optical data.

1.1. The Need for a Uniform Sample

Many studies have investigated the relationships between gas and stars in galaxies (e.g., Roberts 1963; Fisher & Tully 1981; Scodeggio & Gavazzi 1993; Kennicutt et al. 1994; McGaugh & de Blok 1997; Haynes et al. 1999; Burkholder et al. 2001; Swaters et al. 2002; Iglesias-Páramo et al. 2003; Karachentsev et al. 2004; Helmboldt et al. 2004; Rosenberg et al. 2005; Geha et al. 2006; Serra et al. 2007; Walter et al. 2008; Disney et al. 2008; Zhang et al. 2009). However, many of these have relied on small inhomogeneous samples. These studies have been sufficient to establish the broad trend of increasing gas-richness in low-mass systems, but they are limited in their ability to constrain more accurate relationships between gas, stars, and galaxy mass, as well as the intrinsic scatter in these physical quantities. The advent of large astronomical surveys allows for unions of these large surveys to yield multi-wavelength, uniform data sets with small systemic errors and large sample sizes (e.g., Salim et al. 2005; Agüeros et al. 2005; Obrić et al. 2006; Covey et al. 2008).

As mentioned above, several studies have combined large H I surveys with large optical and infrared data sets. In the first of these, Rosenberg et al. (2005) investigated how the infrared stellar light compares to the H I gas emission. Although Rosenberg et al. (2005) were able to probe the baryonic content of a large sample of galaxies, they were limited by the shallow depth of 2MASS, which does not have data for many of the LSB galaxies in the sample. Their study therefore excludes the galaxies at the extreme gas-rich end of the evolutionary spectrum. Another large-scale blind H I survey is the HIPASS (Barnes et al. 2001; Meyer et al. 2004; Zwaan et al. 2004; Wong et al. 2006), which has been combined with IR and optical catalogs (Doyle et al. 2005; Wong et al. 2009) that are very similar to our ES/SDSS catalog (see below). In fact, a large fraction of the ES data are in the HIPASS catalog (see Garcia-Appadoo et al. 2009 for more information). While the HIPASS studies have much more sky coverage than our ES/SDSS catalog, the depth of the SDSS allows us to probe optical magnitudes several times fainter and recover optical counterparts for all of the H I sources in our footprint.

The union of SDSS and the ES provides the desired uniformity in both the optical and the radio (HI) data, along with remarkable depth and dynamic range of the optical SDSS data. Although there is only a modest area of SDSS/ES overlap, enough data exist for the construction of a uniform H I-selected catalog that can be used to probe how the baryonic content of galaxies changes as a function of other physical parameters.

This paper is one of several papers utilizing the combined ES/SDSS data. In this paper, we describe the sample selection, discuss the methods by which we derive the optical photometric parameters, and present the optical data. We briefly describe the sample characteristics and compare our sample to an optically selected sample in a similar volume. Other papers describe the H I data (Garcia-Appadoo et al. 2009) and explore the gas fractions, colors (West et al. 2009), and dynamics of the ES/SDSS galaxies.

2. SURVEY DESCRIPTIONS AND SAMPLE SELECTION

2.1. Equatorial Survey

The ES was carried out with the Parkes Multibeam system on the 64 m radio telescope in Parkes, Australia (Staveley-Smith et al. 1996). The ES, which is described in detail in an accompanying paper (Garcia-Appadoo et al. 2009), circles the celestial equator between $-6 < \delta < +10$ and contains over 1000 sources in 5738 square degrees. The raw data form part of HIPASS (Barnes et al. 2001; Meyer et al. 2004; Zwaan et al. 2004; Wong et al. 2006), carried out with the same instrument over the entire sky between $-90 < \delta < +25$. However, the ES fields were searched much earlier (Garcia-Appadoo et al. 2009) in readiness for comparison with the earliest SDSS data. While the search techniques were much the same as the HIPASS team's and rely heavily on their procedures, the source lists are not identical. For example, the completeness limit of the ES list is 30% fainter than the HIPASS limit. This is mainly due to our ability to follow up and confirm a higher proportion of the fainter sources, a process that would be impractical with the larger survey. Garcia-Appadoo et al. (2009) include a more detailed comparison between HIPASS and the ES.

The ES covers a velocity range from -1280 to 12700 km s^{-1} with an RMS noise of 13 mJy. The velocity resolution of the ES H I spectra is 18.0 km s^{-1} and the 3σ H I mass limit of the survey is $10^6 \times D^2_{\rm Mpc}\, M_\odot$, assuming a 200 km s^{-1} H I galaxy profile. For detailed descriptions of the data acquisition, calibration, and reliability see Garcia-Appadoo et al. (2009) and the HIPASS analysis contained in Barnes et al. (2001), Meyer et al. (2004), and Zwaan et al. (2004).

The ES data cubes were searched using an automated search code written in `MIRIAD`. One thousand one hundred sixty four sources were extracted from regions of the sky where SDSS overlaps were likely to occur. For each source detection, the H I spectrum was extracted by fitting a baseline to the background flux (Barnes et al. 2001). The source position, recessional velocity, 20% peak velocity width, peak and integrated fluxes were measured from the spectrum. For further details on the H I source extraction and parameter measurements for the ES-SDSS sample, see the description in Garcia-Appadoo et al. (2009).

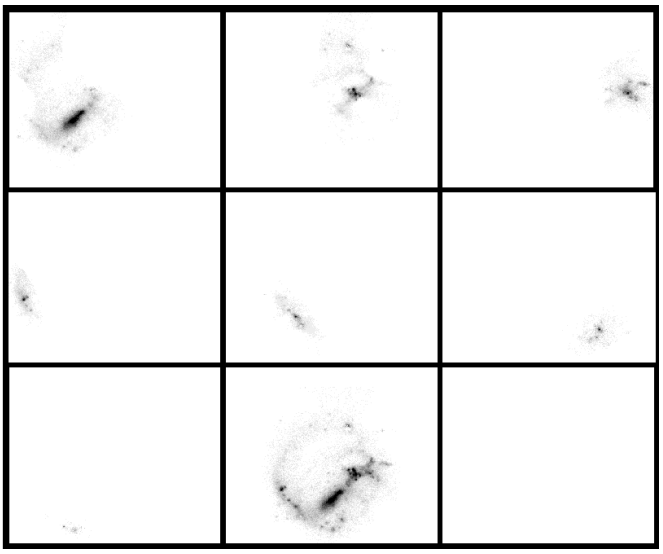

Figure 1. *r*-band atlas images for HIPEQ1124+03. The deblender has divided this galaxy into seven children. The "brightest child" (upper left) contains only 50% of the total galaxy flux. The irregular morphology of this system is responsible for the large degree of "shredding'." The combined image is in the lower-middle panel.

2.2. SDSS Survey

The optical data for this study come from the SDSS Data Release 2 (DR2; Abazajian et al. 2004) sky area. The DR2 area is 3324 deg^2, ∼1700 deg^2 of which overlaps with the 5738 square degree ES region discussed above. The majority of the overlap falls along the $\delta = 0$ strip (excluding the Galactic plane) and the DR2 coverage of the northern Galactic cap ($-5 \lesssim \delta \lesssim 5$; see Garcia-Appadoo et al. 2009 for further details). Automatic pipelines (Pier et al. 2003; Lupton et al. 2002) reduce the raw data and store the derived quantities in a catalog. The SDSS photometric pipeline (PHOTO; Lupton et al. 2002) is optimized for speed and the faint end of galaxy population. Galaxies in the tail of angular size distribution (large) and surface brightness distribution (low) often have unreliable measurements (see Section 2.3). Therefore, aside from the initial catalog matching described below, no SDSS catalog data were used for this study. All photometric quantities were obtained using a new set of techniques optimized for deriving large galaxy photometry.

2.3. Deblending and Sky Subtraction in SDSS

The SDSS automatic pipelines were optimized for angularly small, faint objects. It was found that the SDSS catalog values for angularly large, bright galaxies are often unreliable. Before we re-derive the photometric values for the ES/SDSS sample, we will briefly discuss and quantify two of the problems with large, bright galaxies in the SDSS, namely issues with deblending (or shredding), and sky subtraction. Both of these problems have been discussed in previous papers (e.g., Abazajian et al. 2004, 2009) but require additional attention as they have particular relevance for the ES/SDSS sample.

The SDSS photometric pipeline (PHOTO; Lupton et al. 2002) identifies objects in SDSS fields and extracts them into individual atlas images for photometric analysis. When one object falls in front (or near) another on an SDSS field, the parent images are sent to the deblender. The deblender separates the two objects into children, and photometry is performed on both images independently. For most objects in SDSS, this process works well.

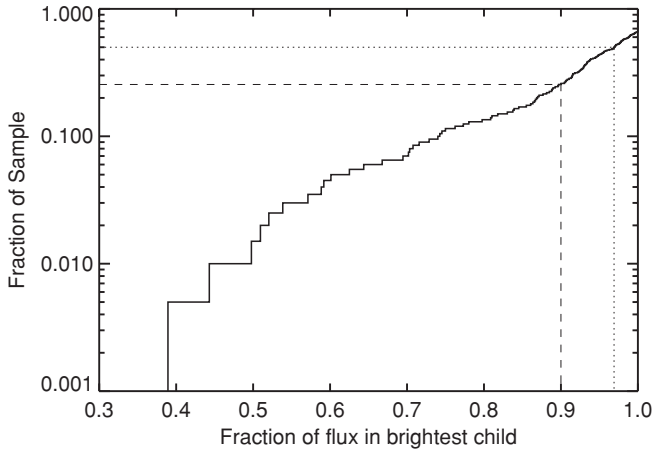

Figure 2. Cumulative distribution of the fraction of flux in the brightest child of deblended ES/SDSS galaxies. The dashed line indicates the level at which galaxies have at least 90% of their flux contained in the brightest child. This accounts for more than 75% of the total sample. The dotted line shows the median value of the sample. Half of the objects have brightest children with more than 96% of the total flux.

However, in galaxies with large angular extent, irregular morphology or LSB, PHOTO deblends more children than it should; H II regions and spiral arms are frequently separated from their parent galaxies. Because these galaxies are "shredded" into multiple pieces, accurate photometry is prohibited by the standard photometric pipeline.

Using the ES/SDSS sample, we demonstrate the amplitude of the deblending problems in the SDSS catalog. Some of the galaxies deblend perfectly; no significant amount of flux has been removed, and the foreground stars have been correctly deblended. However, in some cases, the deblending is quite extreme. Figure 1 shows the seven children that were shredded off of the ES/SDSS source HIPEQ1124+03. The aggressive deblending resulted in the brightest child (upper left) only containing 50% of the of total flux. The SDSS catalog photometry for HIPEQ1124+03 is therefore completely unreliable. We quantified the magnitude of the deblending problem in the ES/SDSS sample by examining the fraction of flux in the brightest child for each of the ES/SDSS galaxies. Figure 2 shows a cumulative distribution of the fraction of flux contained in the brightest child for the ES/SDSS sample. Roughly 75% of the galaxies have more than 90% of their flux contained in the brightest child. The remaining 25% have irregular morphologies, are flocculant (H II regions are removed as stars), or have LSB, with a number of brightest children having less than 50% of the total galaxy flux. We discuss our method for remedying the deblending problems in the ES/SDSS sample in Section 4.1.

Problems with the sky subtraction for bright SDSS galaxies have been recently identified in the literature (Mandelbaum et al. 2005; Bernardi 2007; Lauer et al. 2007; Adelman-McCarthy et al. 2008; Abazajian et al. 2009). Previous simulations indicate that the magnitude of the sky subtraction error can be as high as 0.4 mag (Masjedi et al. 2006; Abazajian et al. 2009). Like deblending, the sky subtraction algorithm (see Lupton et al. 2002) is optimized for small, faint objects and uses a 256 × 256 pixel mask to determine the sky value in 128 pixel intervals across an SDSS field. If a galaxy in the field takes up an appreciable fraction of the mask, the sky is overestimated (and oversubtracted). Therefore, we find that angular size, and not magnitude is the main determiner of sky subtraction

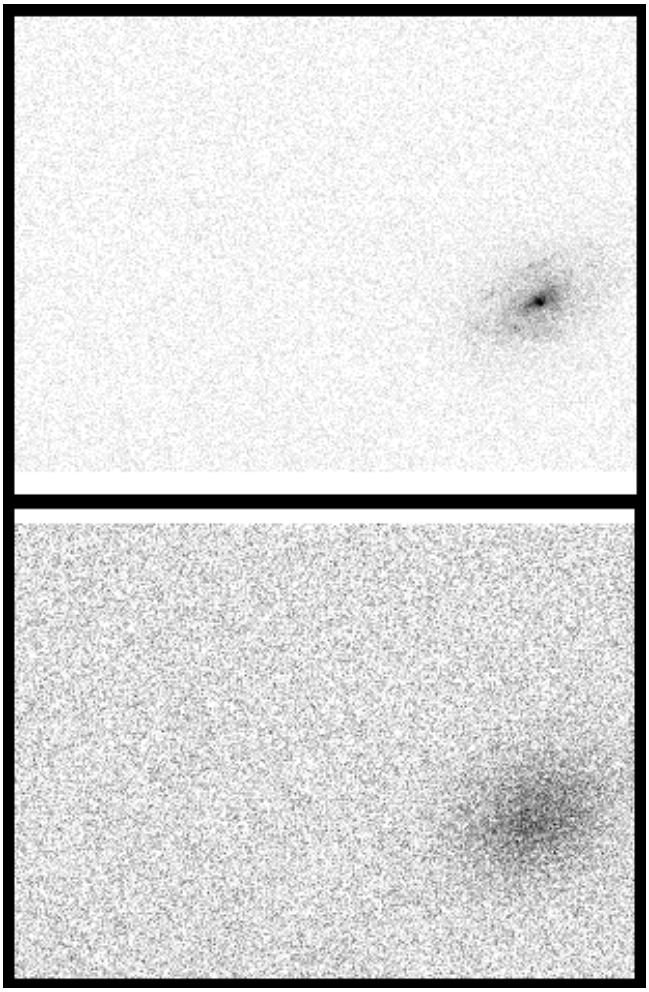

Figure 3. Reconstructed Field for HIPEQ1232+00a with only the relevant atlas images included in the field (top). Rebuilt PHOTO sky for galaxy HIPEQ1232+00a (bottom). The bottom field is what PHOTO subtracted from the corrected frame before photometry was performed. Flux from the galaxy is clearly seen on this image, highlighting the overestimation of sky for large, bright galaxies.

error. Figure 3 shows a reconstructed SDSS field (top; see Section 4.1) and the rebuilt sky (bottom) for ES/SDSS source HIPEQ1232+00a. An accurate sky determination should yield a smooth surface. However, the bottom panel clearly contains flux from the galaxy, which results in fainter magnitudes when it is subtracted from the top image.

To investigate the magnitude of the sky subtraction problem for the ES/SDSS sample, we ran our photometric software (see Section 4.4) on the ES/SDSS galaxies with both the standard SDSS sky subtraction and our sky determination (see Section 4.2) and compared the results. Figure 4 shows the difference in r-band magnitude between the two sky subtraction methods for all of the ES/SDSS galaxies as a function of the area of the galaxy (determined at the 90% light radius). While the effect is negligible for small galaxies (<0.5 □′), galaxies with angular areas of ∼1 □′ have magnitude errors greater than 0.2 magnitudes. There are several galaxies in the ES/SDSS sample where the magnitude error from sky subtraction is larger than 1 mag.

The scatter in Figure 4 implies that other parameters beyond angular size affect the flux lost to sky subtraction errors. Instead of looking at the magnitude difference (which is fractional flux), we explored the actual flux lost as a function of galaxy size,

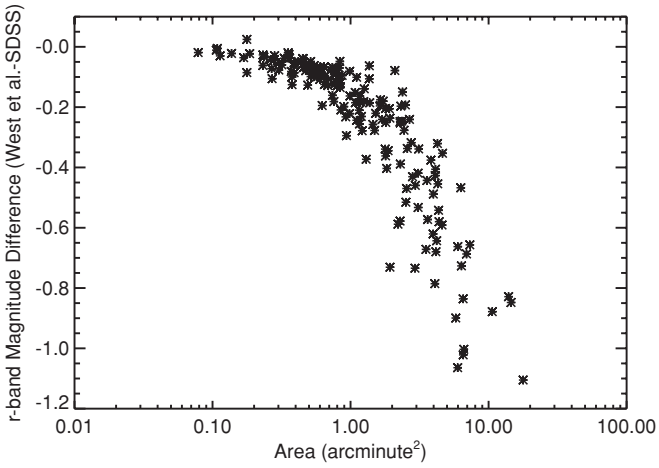

Figure 4. Difference between the r-band magnitude derived using our sky subtraction pipeline and that of SDSS as a function of the area with the PetroR90 radius for the ES/SDSS sample. For galaxies with areas larger than 0.5 □′, the loss from bad sky subtraction is substantial.

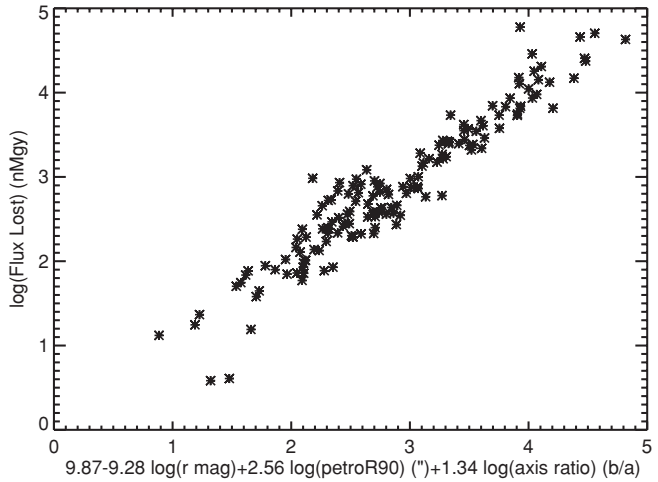

Figure 5. Projection of the best-fit hyperplane to log (m_r), log (petroR90), log (axis ratio), and log (flux lost) for the ES/SDSS galaxies. The scatter is less than half of an order of magnitude. The same relation applies to each of the other four bandpasses.

magnitude, and axis ratio. The larger galaxies fill more of the sky mask, resulting in more of their flux being subtracted. But the amount of flux depends on the surface brightness of the source (which depends on magnitude, area, and axis ratio).

We fit a hyperplane to the logarithms of the flux lost (in nanomaggies[10]; Blanton et al. 2003b), the r-band magnitudes, the Petrosian 90% light radii, and the axis ratios (all measured using the SDSS catalog values). Figure 5 shows the projection of the best-fit hyperplane for all of the ES/SDSS galaxies and can be described by

$$\log(\mathrm{flux}_{\mathrm{lost}}) = 9.87 - 9.28\log(m_r) + 2.56\log(\mathrm{petro}R90) + 1.34\log(b/a) \pm 0.23, \quad (1)$$

where the flux is measured in units of nanomaggies, petro$R$90 is the SDSS Petrosian 90% light radius measured in arcseconds, and b/a is the axis ratio of the galaxy. The axis ratio (b/a) is determined from the major and minor axes derived from SDSS

[10] Nanomaggies (nMgy) are a standardized flux unit where $m = 22.5–2.5\log(\mathrm{nMgy})$.

isophotal photometry (`isoA` and `isoB` in `PHOTO` respectively). Future analysis of bright, angularly large galaxies in SDSS can be corrected at the catalog level using Equation (1). However, for the ES/SDSS sample, we will use our sky subtraction method that is described below (Section 4.2).

2.4. Comparison Sample

To compare the H I-selected ES/SDSS galaxies to an optically selected sample, we use the Data Release 4 (DR4; Adelman-McCarthy et al. 2006) "main" galaxy sample with $m_{r,\mathrm{Petrosian}} < 17.77$ mag. (Strauss et al. 2002). We apply a secondary cut of $z < 0.04$ to ensure that a small local volume is being sampled. There are 30,236 SDSS galaxies in this volume that we will use for comparison. Because there were no major photometry changes between DR4 and DR2, there is no concern in comparing the DR4 data of our main comparison sample to our ES/SDSS sample drawn from DR2. Because of the surface brightness limit for SDSS spectroscopic observations (Strauss et al. 2002), the comparison sample does not contain any galaxies with $\mu_r > 23.0$, where μ_r is the Petrosian surface brightness (within the 50% radius).

The comparison sample serves two distinct purposes: (1) to highlight the fact that an H I-selected sample selects a different subset of galaxies than are available in the SDSS spectroscopic catalog and (2) to compare the properties of an optically selected sample to those of an H I-selected sample. The latter requires that we constrain our comparisons to galaxies that fall within the same volume. There are 51 ES/SDSS galaxies and 18,379 SDSS "main" galaxies in the overlapping volume.

2.5. Matching/Confirmation

2.5.1. SDSS Photometry

The catalog matching began by searching the DR2 `tsObj` files for all SDSS sources within 10′ of the ES source positions. A web page showing the field for each matching SDSS object was created, and all candidate objects were sorted by inverse object size (large to small) to ease visual inspection. Over 1.16 million SDSS objects were found inside the beam areas of 310 ES sources that fell within the SDSS DR2 footprint. At every ES source position, the candidate SDSS objects were visually inspected and potential counterpart galaxies identified.

To be included in the ES/SDSS sample, each candidate galaxy had to meet four criteria: (1) the ES recessional velocity must agree to within twice the W_{20} value of the optically derived redshift, (2) there must be no more than one detectable spatially resolved galaxy within the ES beam at the same redshift, (3) the candidate galaxy must not extend across two or more SDSS fields, and (4) all galaxies must be at least 1′ away from any saturated foreground stars.

To apply the first criterion, we obtained a redshift for each candidate galaxy. SDSS spectra and redshifts were available for ∼80% of the candidate galaxies. For the remaining candidates, we searched the NED[11] database and acquired redshifts for all but ∼20 galaxies. The remaining sources were spectroscopically observed using the Apache Point Observatory's (APO) ARC 3.5 m telescope from 2002 February to 2003 July. All of the sources were observed with long integrations (>20 minutes) on the Dual Imaging Spectrograph (DIS) with a 1.″5 slit and with the high-resolution gratings (∼2 Å). Most of the galaxies in the ES/SDSS sample are currently forming stars and have emission lines that can be unambiguously identified and easily measured for accurate redshift determination. Most of the galaxies have H I and optical recessional velocities that match to within half of the H I line width (see Figure 10 of Garcia-Appadoo et al. 2009). After obtaining redshifts for all of the candidate sources, *all* 310 ES sources in the DR2 footprint had SDSS galaxies within the ES beam at the same redshift.

Of these 310 galaxies, 90 failed the second criterion due to multiple SDSS galaxies within a single ES beam. Some of the H I detections had as many as five galaxies at the same redshift, making it impossible to assign an H I mass to an individual galaxy. With multiple galaxies in the ES beam, only the total H I of the group is measured, and without higher resolution 21 cm observations, this problem cannot be resolved. This may introduce a bias against galaxies in higher density regions when determining the H I mass function from the combined ES/SDSS sample.

At the time of sample selection, no techniques were available to accurately obtain the photometry for galaxies with flux spread over multiple fields. Twenty of the galaxies were positioned in such a way and/or had angular extents so large that they fell over multiple SDSS fields (criterion 3) and were therefore excluded from our catalog. This selection criteria also introduces a bias against the largest nearby galaxies.

Five additional galaxies were removed because of their close proximity to saturated foreground stars (criterion 4) whose scattered light would greatly effect galaxy photometry. Since the superposition of stars in front of galaxies is random, this criterion should not introduce any additional bias.

The resulting ES/SDSS sample consists of the 195 galaxies that passed all four criteria. Their survey names, central SDSS positions, other catalog names, and morphological types from NED can be found in Table 1.[12] The position centers are those used for photometry. We refer to objects both in the text and in tables by their ES (HIPEQ) catalog name.

3. DISTANCE

Because of the limits of the ES survey, the H I-selected sample probes only the very nearby universe. Figure 6 shows the redshift distribution of the H I-selected galaxies (solid) with the redshift distribution of a volume-limited sample of SDSS galaxies (dotted) from the DR4 main galaxy sample. The galaxies in the H I-selected sample are clearly biased toward very small distances, compared to the galaxies included in most SDSS studies. Although this means that the H I-selected sample probes a smaller volume than other SDSS studies, the volume it samples is more complete because it includes substantial LSB and low luminosity populations (although the sample is still missing gas-free galaxies eliminated by the selection criteria).

Many measured recessional velocities are likely to be influenced by infall toward Virgo. We adopt a cosmology with $H_0 = 70$ km s^{-1} Mpc^{-1}, $\Omega_M = 0.3$, and $\Omega_\Lambda = 0.7$ and then correct recessional velocities for Virgo infall using the `IDL` routine `v_converter`, which derives velocity corrections from the LEDA database (Theureau et al. 1998; Terry et al. 2002). The velocities are then converted into redshifts and luminosity distance. The adopted distances can be found in Table 4.

[11] This research has made use of the NASA/IPAC Extragalactic Database (NED) which is operated by the Jet Propulsion Laboratory, California Institute of Technology, under contract with the National Aeronautics and Space Administration.

[12] All measured and derived photometric quantities for the ES/SDSS sample can be obtained electronically using the CDS Vizier database http://vizier.u-strasbg.fr/viz-bin/VizieR.

Table 1
Galaxy Names

ES Name	R.A. (J2000)			Decl. (J2000)			Other Name[a]	SDSS Name	Morphological Type[a]
	h	m	s	°	′	″			
HIPEQ0014−00	00	14	31.87	−00	44	15.0	UGC00139	SDSS J001431.87−004415.0	SAB(s)c
HIPEQ0027−01a	00	27	49.46	−01	11	60.0	UGC00272	SDSS J002749.46−011160.0	SAB(s)d
HIPEQ0033−01	00	33	21.96	−01	07	18.8	UGC00328	SDSS J003321.96−010718.8	SB(rs)dm
HIPEQ0043−00	00	43	27.77	−00	07	30.4	NGC0237	SDSS J004327.77−000730.4	SAB(rs)cd
HIPEQ0051−00	00	51	59.59	−00	29	11.8	ARK018	SDSS J005159.59−002911.8	Sb
HIPEQ0058 + 00	00	58	48.82	+00	35	12.1	IC1607/UGC00611	SDSS J005848.82 + 003512.1	Sb
HIPEQ0107 + 01	01	07	46.30	+01	03	49.0	UGC00695	SDSS J010746.30 + 010349.0	Sc
HIPEQ0119 + 00	01	19	58.78	+00	43	18.5	LSBC_F827−05	SDSS J011958.78 + 004318.5	Sd
HIPEQ0120−00	01	20	06.58	−00	12	19.1	UGC00866	SDSS J012006.58−001219.1	Sdm
HIPEQ0122 + 00	01	22	09.10	+00	56	44.9	NGC0493	SDSS J012209.10 + 005644.9	SAB(s)cd

Note. [a] Name and morphological-type information obtained from NED.

(This table is available in its entirety in machine-readable and Virtual Observatory (VO) forms in the online journal. A portion is shown here for guidance regarding its form and content.)

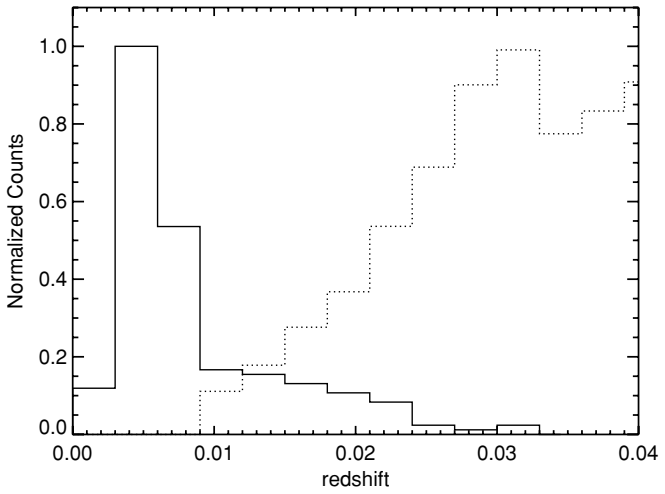

Figure 6. Redshift distribution of the H I-selected galaxies (solid) and of a volume-limited sample of SDSS galaxies (dotted) from the Data Release 4 (DR4) main galaxy sample. The H I-selected galaxies are much closer than those in most SDSS galaxy studies. (A similar figure using recessional velocity in place of redshift was included in the Garcia-Appadoo et al. 2009 paper).

4. H I-SELECTED GALAXIES—PHOTOMETRY

SDSS photometry of large galaxies is non-trivial. In almost every SDSS galaxy study to date, large, nearby galaxies have been purposefully avoided because of the challenge in correctly extracting their photometric quantities. Problems with deblending and sky subtraction preclude an automated catalog-level analysis of large galaxies, and the inclination problems in the Petrosian quantities derived by SDSS adversely affect the photometry of both large and small galaxies (Bailin & Harris 2008). In this section, we discuss the limitations of SDSS photometry and outline the methods used to remedy the situation. We then apply these techniques to derive photometry for the ES/SDSS sample.

4.1. Creating New Atlas Images

4.1.1. Reconstruction of Atlas Images

For each galaxy in the ES/SDSS sample, we downloaded all atlas images within a 5′ radius of the galaxy center. We visually inspected each atlas image and identified the children that belonged to the ES/SDSS galaxy. For the most part, the appropriate children were easy to identify because of their uniform colors and extended morphology. In a few cases, however, confusion between an H II region and a foreground star made the choice difficult. In these cases, we examined the colors of the star-like objects and included them as children if they fell off the stellar locus as defined by Covey et al. (2007). The `object_id` for likely parts of the galaxies were saved, and the corresponding images were mosaicked together to reconstruct an image uncontaminated by stars. The reconstructed image was visually inspected to ensure that it did not have significant missing children and that bright stars and their artifacts were not included in the reconstructed images.

To properly reconstruct the images of the galaxies with their original sky, we used the `tsObj`, `fpAtlas`, `fpBIN` and `fpFieldStat` SDSS files to rebuild corrected frames (`fpC` files) from a specified list of atlas images. The resulting images contain only the galaxy superimposed on a restored image of the sky. We also reconstructed single galaxy `fpC` files and sky images for every field. The latter were useful in correcting for the error in the SDSS sky subtraction (see Section 4.2 below).

Finally, we aligned all five SDSS bands to the same pixel coordinates and made cut-outs of each galaxy while preserving the astrometric (and other header) information.

4.1.2. Masking Out Stars

Twelve of the galaxies in the sample were so badly deblended by `PHOTO` that they could not be easily reconstructed from their deblended children. Instead, we created a sky-subtracted `fpC` file of the deblended parent galaxy. To remove the stars from the atlas images, we masked out the bright stars and filled in the masked regions by interpolating from surrounding pixels.

4.2. Sky Subtraction

4.2.1. Sky Subtraction of SDSS Fields

As outlined above, sky subtraction errors for large galaxies can be larger than 1 mag in the SDSS catalog data. These errors are significant and must be avoided for the large galaxies (area $> 0.5\square'$) that dominate our sample.

To subtract the sky from our images, we followed the procedure outlined below. We ran `SExtractor` (Bertin & Arnouts 1996) on an *r*-band subregion of a corrected frame (`fpC` file) to identify sources and masked all non-sky pixels, growing masks where needed to eliminate all galaxy flux

from sky regions. Then we fit a tilted plane to the remaining sky pixels and subtracted the tilted plane fit from the reconstructed galaxy image. We repeated this procedure for all five bands (u, g, r, i, z) using the masks derived from the r-band subregion.

4.2.2. Verifying Sky Subtraction Accuracy

Many of the sources in our catalog have very low surface brightness, making their photometry particularly sensitive to errors in sky subtraction. Unlike random errors due to dark current and Poisson noise, errors in sky determination lead to systematic oversubtraction or undersubtraction of flux from every pixel in a galaxy image. Thus, errors in the sky level do not average to zero over a galaxy image, and instead can be a major source of uncertainty, particularly for large and/or low surface brightness galaxies. In this section, we explore various methods of calculating the sky background and show that almost all of the methods return similar results. We used the differences among sky subtraction techniques to characterize the uncertainty in determining the sky background.

We selected a sparsely populated field from the SDSS on which to test various sky subtraction methods. We tested 12 different methods using the combination of three different sky field cutouts and four different parameterizations for the shape of the sky background surface fits, ranging from first order (i.e., a tilted plane) to fourth order (i.e., a fourth-order polynomial in x and y), respectively. The different sky fields are: (1) an SDSS field ($13' \times 9'$) with all of the objects masked out, (2) an SDSS field with all of the objects masked out and the mask of HIPEQ0014-00 (a medium/large-sized galaxy in the sample with an area of 1.4 arcmin^2) superimposed on the field (this additional masking leaves a large "hole" in the image at the galaxy location, adding uncertainty to the fitting procedure), and (3) a $4' \times 5'$ subregion of an SDSS field with all of the objects masked out and the mask of HIPEQ0014-00 superimposed on the cutout. Each of the 12 methods was run on all five bands of the sparsely populated SDSS test image.

To quantify the differences among the various methods, we calculated the average residual counts per pixel in the area under the HIPEQ0014-00 mask corresponding to the area where galaxy photometry would be measured. We assumed that a perfect sky subtraction yields a mean residual sky level of zero. Thus, any non-zero mean sky level is a measure of the sky subtraction uncertainty, and is reported as the residual. This analysis adequately reproduces the manner in which actual sky subtraction of a galaxy field is calculated and assesses the relevant residuals that affect galaxy photometry.

The maximum residual in any of the five bands is 0.1 counts pixel^{-1} and the RMS is 0.04 counts pixel^{-1}. For an $m_r \sim 13$ galaxy with an aperture area of $4\square'$, a residual of 0.1 count pixel^{-1} results in a $0\overset{m}{.}01$ change. For comparison, a residual of 1 count pixel^{-1} would result in a $0\overset{m}{.}2$ change for the same galaxy. The residuals show no clear trend with either the fit order or the area schema. However, the i-band data have systematically larger residuals while the z-band's are systematically smaller. This may be due to faint red objects that are unidentified in the r band, detected in i and marginally detected in z (which is substantially shallower than i). These objects would not be properly removed using the r-band masks.

All of the methods have residuals that are well below other per pixel uncertainties that will be described below (e.g. the `Dark Variance` varies between 0.9 and 3.9 counts pixel^{-1}). Therefore, we conclude that choosing any of these methods will not have an effect of more than $\sim 0\overset{m}{.}01$ on the resulting photometry.

For the photometry presented in this study, we have adopted a tilted plane fit to a subregion of the SDSS field for the sky subtraction. This approach is the computationally fastest method and, although the z-band residual is slightly worse than other methods, the deviation is still not significant. For completeness, we use the largest absolute residual in each band (regardless of method) as a measure of the uncertainty in the sky value. This is added to the uncertainty analysis described below.

We note that the SDSS residual (defined as the mean difference between the SDSS sky and the method presented in this paper) for ES/SDSS galaxy HIPEQ0014-00 is $\sim$1.13 counts pixel^{-1}, demonstrating the improvement made over the SDSS pipeline sky subtraction. The improved sky subtraction changes the r-band magnitude of HIPEQ0014-00 by 0.19 mag.

4.3. Model Fitting

The reconstructed sky-subtracted galaxy images were run through two different model-fitting routines to quantify the galaxies' sizes, surface brightnesses, and orientations. Both fitting routines use the Levenberg–Marquardt (LM) minimization technique to calculate a two-dimensional surface fit to a galaxy image. The first routine fits a single Sérsic (1968) profile, and the second fits a two component, double exponential disk. All fits were performed on the r-band images. If the fit was able to accurately reproduce the galaxy image, then an elliptical aperture was used for subsequent photometry. Forty-seven galaxies were not well fit by this simple profile because of their irregular morphologies and/or LSBs. For the irregular and LSB galaxies, the parameters are not reliable, and a default circular aperture is used for photometry. Although the lack of seeing in the models may introduce a small amount of uncertainty into the exact Sérsic profile derived, it has almost no effect on the aperture shape

4.4. Petrosian Photometry

In this section, we discuss the derivation of Petrosian quantities for the ES/SDSS sample. Petrosian (1976) photometry recovers a nearly constant fraction of a galaxy's flux for a variety of morphological types and surface brightness profiles. The resulting photometry has fewer biases than those that estimate the total galaxy flux with apertures based on isophotes or fractions of the central surface brightness. A modified Petrosian photometric system has been adopted by SDSS (see Blanton et al. 2001; Yasuda et al. 2001).

Petrosian quantities were adopted for this study to be consistent with SDSS photometry, allowing us to compare our results to the greater SDSS sample. The SDSS photometric pipeline uses circular apertures to extract Petrosian quantities. However, this produces a significant inclination dependence in some of the resulting photometric quantities (Bailin & Harris 2008). This bias is worse in our sample than the Main SDSS sample because the ES/SDSS galaxies are sufficiently nearby that their inclinations are unaffected by seeing (which tends to circularize angularly small galaxies). We have remedied this problem by allowing for elliptical apertures in our Petrosian photometric pipeline. For the galaxies with high-quality Sérsic fits, we adapted the SDSS photometric methods to include elliptically shaped photometric apertures. We also measured every galaxy with a circular aperture for

Table 2
Petrosian Photometry of H I Selected Sources

ES Name	R.A. (J2000)[c]	Decl. (J2000)[c]	u	g	r	i	z	PetroR50 ($''$)	PetroR90 ($''$)
HIPEQ0014−00[a]	3.63280	−0.7375	14.88 ± 0.04	13.92 ± 0.01	13.47 ± 0.02	13.28 ± 0.01	13.06 ± 0.03	21.4 ± 0.4	59.0 ± 0.8
HIPEQ0027−01a[a]	6.95610	−1.2000	15.65 ± 0.04	14.75 ± 0.01	14.32 ± 0.02	14.16 ± 0.01	14.10 ± 0.04	21.4 ± 0.4	43.6 ± 0.8
HIPEQ0033−01[b]	8.34150	−1.1219	16.06 ± 0.06	15.15 ± 0.01	14.78 ± 0.02	14.61 ± 0.01	14.49 ± 0.05	20.2 ± 0.4	45.9 ± 1.6
HIPEQ0043−00[a]	10.86570	−0.1251	14.50 ± 0.03	13.37 ± 0.01	12.82 ± 0.02	12.55 ± 0.01	12.29 ± 0.03	13.9 ± 0.4	36.4 ± 0.4
HIPEQ0051−00[a]	12.99830	−0.4866	16.08 ± 0.03	15.08 ± 0.01	14.56 ± 0.02	14.34 ± 0.01	14.17 ± 0.03	6.3 ± 0.4	17.4 ± 0.4
HIPEQ0058 + 00[a]	14.70340	0.5867	15.14 ± 0.03	14.06 ± 0.01	13.53 ± 0.02	13.29 ± 0.01	13.11 ± 0.03	10.7 ± 0.4	23.0 ± 0.4
HIPEQ0107 + 01[b]	16.94290	1.0636	15.95 ± 0.04	15.07 ± 0.01	14.74 ± 0.02	14.61 ± 0.01	14.55 ± 0.04	10.7 ± 0.4	26.5 ± 0.8
HIPEQ0119 + 00[b]	19.99490	0.7218	18.02 ± 0.11	17.17 ± 0.02	16.80 ± 0.03	16.66 ± 0.03	16.50 ± 0.10	7.1 ± 0.4	15.4 ± 2.0
HIPEQ0120−00[a]	20.02740	−0.2053	16.27 ± 0.04	15.33 ± 0.01	14.88 ± 0.02	14.70 ± 0.01	14.53 ± 0.04	18.2 ± 0.4	35.6 ± 0.8
HIPEQ0122 + 00[a]	20.53790	0.9458	13.68 ± 0.03	12.80 ± 0.01	12.38 ± 0.02	12.11 ± 0.01	11.87 ± 0.03	53.5 ± 0.4	105.7 ± 0.8

Notes.
[a] Photometry was derived using an elliptical aperture.
[b] Photometry was derived using a circular aperture.
[c] R.A. and decl. given in decimal degrees.

(This table is available in its entirety in machine-readable and Virtual Observatory (VO) forms in the online journal. A portion is shown here for guidance regarding its form and content.)

comparison with standard SDSS outputs. These circular measurements were adopted for galaxies whose Sérsic fits were of poor quality.

The first step in deriving Petrosian quantities was to calculate the Petrosian radius. Following the SDSS prescription, we defined the Petrosian ratio R_P as

$$R_P(r) \equiv \frac{\int_{0.8r}^{1.25r} dr' 2\pi r' I(r')/[\pi(1.25^2–0.8^2)r^2]}{\int_0^r dr' 2\pi r' I(r')/(\pi r^2)}, \quad (2)$$

where $I(r)$ is the azimuthally averaged surface brightness profile. We performed the integration by taking one pixel steps and calculating the subsequent Petrosian ratio at every pixel from the galaxy center. In the SDSS pipeline, the Petrosian radius r_P is defined as the radius at which $R_P(r)$ is equal to 0.2 (see Blanton et al. 2001; Yasuda et al. 2001). The Petrosian flux f_P in any band was then defined as the flux within 2.0 Petrosian radii:

$$f_P \equiv \int_0^{2r_P} 2\pi r' I(r') dr'. \quad (3)$$

Our method differs from the SDSS method in that we use elliptical apertures in addition to the standard SDSS circular apertures.

To correctly measure colors of the galaxies, the magnitude determination for all five bands must use the same aperture. Mimicking SDSS, we used the derived r-band aperture for all bands.

In some cases, the Petrosian radius was so large that the derived aperture (r_P) far exceeded the observed boundaries of the galaxy. In these cases, large amounts of sky pixels were included in the galaxy flux. Although in the ideal case, the summation of all sky pixels is zero, we know from Section 4.2 that small residuals exist, and thus, as Petrosian radius increases, so does the error from the sky subtraction residuals. Due to their uncertain, irregular surface brightness profiles, most of the cases where the Petrosian radius was exceedingly large were LSB galaxies. The resulting flux errors were particularly large for these systems because the integrated sky subtraction residuals can be a large fraction of the total galaxy flux. A similar problem is present in the SDSS photometric pipeline (Lupton, private communication). SDSS corrects for this by using the statistically defined edges of atlas images as the maximum possible photometric boundaries. We imposed a similar maximum size for the Petrosian radius using the masks created in sky subtraction for each r-band image as the photometric boundaries (since the aperture is applied to all five bands, this does not affect the measured color of the galaxies). For most of the galaxies, the integration of Petrosian magnitudes rarely reached the mask boundaries, indicating that the galaxy flux was correctly masked out in the sky determination. The only galaxies that reached the mask boundary were the very LSB galaxies, whose Petrosian radii were not well defined (29% of the ES/SDSS sample). Typically, the resulting flux errors from this were only 1% –2% and were propagated into the reported magnitude uncertainties.

Once a Petrosian flux was calculated, we converted all fluxes to asinh magnitudes (Lupton et al. 1999) using the relation

$$\text{mag} = -\frac{2.5}{\ln(10)}\left[\text{asinh}\left(\left(\frac{f}{f_0}\right)/2b\right) + \ln(b)\right], \quad (4)$$

where b is the softening parameter (a constant for each filter), and $\frac{f}{f_0}$ is given by

$$\frac{f}{f_0} = \frac{\text{counts}}{\text{exptime}} 10^{0.4(aa+kk\times\text{airmass})}. \quad (5)$$

Here the aa is the magnitude zero point, measured for each field, kk is the extinction coefficient in magnitudes, and *exptime* is the standard SDSS value of 53.907456 seconds. The values for air mass, aa, and kk were all pulled from the corresponding `tsField` files. Asinh magnitudes were computed for both the elliptical and circular apertures. The resulting magnitudes can be found in Table 2. If a galaxy's profile was not well fit by an elliptical aperture, then the Petrosian circular aperture magnitude was included in Table 2.

For most of the galaxies in the ES/SDSS sample, the main contribution to the photometric uncertainty was dominated by the Poisson noise of the subtracted sky. The Poisson variable for CCD photometry is photo_electrons. We converted from counts to photo_electrons using the following relation:

$$\text{photo\_electrons} = \text{counts} \times \text{gain}, \quad (6)$$

where the gain is a variable quantity that is also stored for each filter in each `field` in the `tsField` files.

Table 3
Corrections to Petrosian Photometry

ES Name	Milky Way Extinction[a]					Internal Extinction[b]					K-correction[c]					Edge
	u	*g*	*r*	*i*	*z*	*u*	*g*	*r*	*i*	*z*	*u*	*g*	*r*	*i*	*z*	Corr.
HIPEQ0014−00	1.09	0.79	0.53	0.46	0.29	0.85	0.62	0.45	0.34	0.24	0.02	−0.01	−0.02	−0.01	−0.02	0.00
HIPEQ0027−01a	0.92	0.65	0.44	0.37	0.23	0.78	0.57	0.42	0.32	0.22	0.02	−0.01	−0.02	−0.01	−0.02	0.00
HIPEQ0033−01	0.39	0.29	0.20	0.17	0.10	0.28	0.20	0.15	0.11	0.08	0.00	0.00	0.00	0.00	−0.01	0.00
HIPEQ0043−00	0.58	0.42	0.29	0.24	0.16	0.48	0.35	0.25	0.19	0.14	0.02	0.01	−0.01	0.00	−0.01	0.00
HIPEQ0051−00	0.65	0.47	0.32	0.29	0.18	0.45	0.33	0.24	0.18	0.13	0.00	0.00	0.00	0.00	0.00	0.00
HIPEQ0058 + 00	0.21	0.16	0.09	0.10	0.05	0.02	0.01	0.01	0.01	0.00	0.02	0.02	0.01	0.00	−0.01	0.00
HIPEQ0107 + 01	0.14	0.11	0.05	0.08	0.04	0.00	0.00	0.00	0.00	0.00	−0.01	0.00	0.00	0.00	0.00	0.00
HIPEQ0119 + 00	0.15	0.12	0.08	0.06	0.04	0.02	0.01	0.01	0.01	0.00	−0.01	−0.01	0.01	−0.01	−0.01	0.00
HIPEQ0120−00	0.57	0.42	0.29	0.26	0.17	0.39	0.28	0.21	0.16	0.11	0.00	0.00	0.00	0.00	−0.01	0.01
HIPEQ0122 + 00	1.51	1.10	0.78	0.63	0.42	1.35	0.99	0.72	0.54	0.39	−0.01	−0.01	−0.01	−0.01	−0.02	0.00

Notes.
[a] Computed using values in Schlegel et al. (1998).
[b] Based on the method of Tully et al. (1998).
[c] Computed using `kcorrect_v3.2` from Blanton et al. (2003b).

(This table is available in its entirety in machine-readable and Virtual Observatory (VO) forms in the online journal. A portion is shown here for guidance regarding its form and content.)

The photometric uncertainty was then derived to be

$$\text{uncertainty(counts)} = \times \sqrt{\frac{\text{counts} + \text{sky}}{\text{gain}} + N_{\text{pix}}(\text{dark\_variance} + \text{skyErr})} \quad (7)$$

where counts is the galaxy flux in counts, sky is the integrated sky flux in the object aperture, N_{pix} is the number of pixels in the object aperture, dark_variance is a combination of the dark current and the read noise per pixel that was found in the `tsField` files and significantly varies from field to field and filter to filter. The $skyErr$ term is the maximum residual from sky subtraction in each of the five band passes. The uncertainties from Equation (7) (in counts) were then converted to magnitudes using Equation (4). In most cases the counts term dominates the total uncertainty.

4.5. Photometric Corrections

Variations in extinction, cosmic redshift, and SDSS field boundaries can lead to significant offsets in the observed colors and magnitudes of galaxies. Thus, various photometric corrections need to be made to responsibly use the aforementioned photometry for science. In this section, we outline the photometric corrections that are important for the ES/SDSS sample.

4.5.1. Edge Corrections

Of the 195 galaxies in the H I-selected sample, 34 galaxies are close to the edge of an SDSS field, but were included in the sample because the majority of their light falls within the SDSS field. The flux lost beyond the edge boundary should not drastically affect the color of a galaxy, but it can change the derived absolute magnitude. The Sérsic fit models can be used to make a reasonable estimate of the flux lost across the field edge.

To correct for the missing flux, we overlaid the Sérsic models for each of the 34 galaxies and masked out any regions that overlapped (leaving only model flux that crosses the SDSS field boundaries). Using the same Petrosian apertures described in Section 4.4, we calculated the flux remaining from the Sérsic models and converted this additional flux to a magnitude correction. Only 23 of the 34 galaxies had any significant flux ($\geqslant$0.01 magnitudes) that was lost across the field edge, and most of the corrections are smaller than 0.1 mag. Because the Sérsic models are only calculated in the *r* band, we assume that a similar fraction of flux is lost in the other bands and use the *r*-band value as a universal magnitude correction. This assumption is reasonable for small corrections but may be incorrect for larger amounts of lost flux in galaxies with large color gradients. The values for the edge correction are included in Table 3.

4.5.2. Extinction

The photometric magnitudes listed in Table 2 are not corrected for either extinction from the Milky Way or internal extinction from the extragalactic object itself. The former is provided by Schlegel et al. (1998; SFD), using dust maps of the Milky Way. The SDSS database provides the extinction values in all five bands at every SDSS pointing. The SFD extinction values are given in Table 3.

The correction for a galaxy's internal extinction is more complicated. The literature gives examples of extinction corrections that have been applied on the basis of Hubble type (Gavazzi & Boselli 1996), rotation speed (Tully et al. 1998), and a type-independent "sandwich model" (Matthews et al. 1999). We followed the method of Tully et al. (1998) and calculated the internal extinction of a face-on galaxy in the *I* band (γ_I), using the equation

$$\gamma_I = 0.92 + 1.63(\log(2V_{\text{rot}}) - 2.5), \quad (8)$$

where $2V_{\text{rot}}$ is set to the inclination corrected W_{20} derived in Garcia-Appadoo et al. (2009). Several of the galaxies do not have well-measured axis ratios and thus do not have well-measured inclinations, making the appropriate value of V_{rot} uncertain. An inclination of 60° (the average inclination in a randomly aligned sample) was assigned to all of these galaxies. The total extinction correction for the inclined galaxy was then calculated from γ_I using

$$A_I = \gamma_I \log\left(\frac{1}{b/a}\right), \quad (9)$$

where b/a is the axis ratio of the galaxy calculated from the Sérsic fits described Section 4.3.

We converted the *I*-band extinction to the SDSS bands using the relations in Schlegel et al. (1998). The extinction values relative to *I* band for *u*, *g*, *r*, *i*, and *z* are: 2.66, 1.95, 1.42, 1.07, and 0.763, respectively. Many of the calculated extinction values for galaxies with uncertain axis ratios were negative, and all of them had values below 0.09 mag in the *I* band. These were converted to 0 before being applied to the galaxy photometry. The extinction values computed for galaxies with uncertain inclinations are therefore unlikely to have produced significant errors in the final photometry. These galaxies are primarily very blue, LSB systems with low metallicities, and are unlikely to have large dust components. All of the internal extinction values are included in Table 3.

4.5.3. K-Corrections

Although this sample of galaxies is nearby, *K*-corrections are small but important for precise photometry of the more distant galaxies in the sample. We used Blanton et al.'s (2003b) `kcorrect_v3.2` to *K*-correct all of the galaxies in the sample to $z = 0$. These corrections are included in Table 3. The median and the maximum *r*-band *k*-corrections are 0.008 and 0.031, respectively. For the *u* band, the median and maximum *k*-corrections are more important at 0.012 and 0.070, respectively.

4.6. Other Measured Petrosian Properties

In addition to providing a measurement of flux, Petrosian quantities can be used to calculate robust measurements of size and surface brightness. In this section, we describe the method used to derive these quantities.

Once a Petrosian flux was measured (see above), we computed the 50% (R50) and 90% (R90) radii for both the elliptical apertures and circular apertures. These values correspond to the `PetroR50` and `PetroR90` parameters in the SDSS `tsObj` files. They were converted to arcseconds using the SDSS pixel scale of $0\farcs396$ pixel^{-1}. The best-fit R50 and R90 values and their uncertainties are reported in Table 2. For an exponential disk galaxy, the R50 and R90 values correspond to 1.668 and 3.816 times the scale length, respectively. For a de Vaucouleurs model, the R50 and R90 correspond to 0.7124 and 2.387 times the effective half-light radius (r_e).

The Petrosian flux and sizes can be used to compute surface brightness for each galaxy. The Petrosian surface brightness is the average surface brightness within R50, defined by taking half of the Petrosian flux and dividing by the elliptical aperture area with a semi-major axis equal to the elliptical R50. For galaxies with well-defined elliptical apertures, this is the most reliable measure of the average surface brightness of the galaxy as it appears in the image. For a face-on exponential disk, the Petrosian surface brightness is 1.118 times the central surface brightness in mag/$\square''$.

5. PHOTOMETRIC SAMPLE

5.1. Derived Quantities

With excellent five-band photometry, it is possible to explore the photometric properties of this H I-selected sample with unprecedented uniformity. In this section, we derive several quantities from the photometric data, give an overview of the sample properties, and highlight some empirical results from the photometry.

Using the distances derived from the Virgo infall model described above, we computed physical sizes and absolute magnitudes for every galaxy, given in Table 4. There are uncertainties in the flow models used to calculate the Virgo infall velocities. When we computed the distances without the Virgo infall corrections, we get values that differ by at most 6% (average deviation of 2%). When we compared our Virgo infall derived distances to those computed in relation to the cosmic-microwave background, we found deviations of ∼13%. We chose a conservative error uncertainty of 13% for our distance estimates and propagated this uncertainty when calculating absolute magnitudes, stellar masses, and physical sizes.

Absolute magnitudes were calculated using the standard distance modulus formula including all photometric corrections (foreground extinction, internal extinction, *K*-corrections). Luminosities can be computed from the tabulated values of absolute magnitude using the solar absolute $ugriz$ magnitudes (6.41, 5.15, 4.67, 4.56, and 4.53 mag, respectively), provided by Bell et al. (2003). We also tabulated the physical R50 and R90 size (kpc) of each galaxy in the *r* band.

To aid in Tully–Fisher and other dynamical studies, we included the inclination and turbulence corrected circular velocity in Table 4. We correct for inclination and turbulence effects in the H I line widths using the equation

$$W_{20,c} = \frac{W_{20} - W_{20,t}}{2} \left(\frac{1 - (b/a)^2}{1 - 0.19^2} \right)^{-1/2}, \quad (10)$$

where b/a is the optically derived axis ratio, $W_{20,t}$ is the turbulence correction, and 0.19 is typical intrinsic axis ratio for spiral galaxies (Pizagno et al. 2005). For $W_{20,t}$, we use the empirically derived value of 8 km s^{-1} from the late-type galaxy study of Begum et al. (2006). Because of the large uncertainties in several of the derived inclinations (galaxies with circular aperture photometry), not all of the velocities could be properly corrected.

To compute stellar masses, we used the method of Bell et al. (2003) to calculate the stellar mass-to-light ratio in the *i* band. Specifically, we used the relation

$$\log(M_*/L_i) = -0.222 + 0.864(g - r) + \log(0.71), \quad (11)$$

where the factor of 0.71 comes from the conversion between Bell et al.'s (2003) "diet Salpeter" and a Kroupa IMF (Pizagno et al. 2005). The $g - r$ color is used to compute the stellar mass-to-light ratio because it is robust against large changes in color when emission lines dominate the galaxy's spectral energy distribution (West et al. 2009). We used the *i*-band magnitude to compute the stellar mass for the same reason; the *i* band has very few emission lines and is a good indicator of the underlying stellar population.

Assuming an *i*-band solar absolute magnitude of 4.56 (Bell et al. 2003), we derived the stellar mass using

$$M_* = M_*/L_i \times 10^{(-(M_i - 4.56)/2.51)}. \quad (12)$$

The stellar masses are given in Table 4.

5.2. Sample Properties

With the photometry and other photometric quantities complete, we briefly examined the global photometric properties of the sample. The ES/SDSS sample selects galaxies that are bluer, less luminous, less massive, and undergoing higher rates of star formation than those in the SDSS main sample. As we discussed above, a large fraction of these differences are based

Table 4
Derived Quantities

ES Name	Distance	Rotational	Log (Stellar Mass)	Absolute Magnitude					R50 (kpc)	R90 (kpc)
	(Mpc)	Velocity (km s^{-1})[a]	($M_\odot$)	*u*	*g*	*r*	*i*	*z*	*r*-band	*r*-band
HIPEQ0014−00	56.5 ± 7.3	159.6 ± 14.0	10.0 ± 0.6	−19.97 ± 0.30	−20.62 ± 0.27	−20.82 ± 0.39	−20.94 ± 0.16	−20.99 ± 0.30	5.85	16.15
HIPEQ0027−01a	55.4 ± 7.2	119.1 ± 13.6	9.6 ± 0.6	−18.98 ± 0.30	−19.62 ± 0.27	−19.84 ± 0.36	−19.93 ± 0.20	−19.85 ± 0.30	5.74	11.70
HIPEQ0033−01	27.9 ± 3.6	··· ···	8.8 ± 0.6	−16.56 ± 0.32	−17.37 ± 0.28	−17.64 ± 0.43	−17.79 ± 0.13	−17.84 ± 0.32	2.73	6.21
HIPEQ0043−00	59.5 ± 7.7	191.6 ± 17.0	10.4 ± 0.6	−19.95 ± 0.30	−20.92 ± 0.27	−21.34 ± 0.49	−21.56 ± 0.06	−21.73 ± 0.30	4.00	10.50
HIPEQ0051−00	22.7 ± 3.0	99.1 ± 14.6	8.8 ± 0.6	−16.35 ± 0.30	−17.18 ± 0.27	−17.54 ± 0.45	−17.72 ± 0.10	−17.79 ± 0.30	0.70	1.92
HIPEQ0058 + 00	77.5 ± 10.1	··· ···	10.3 ± 0.6	−19.51 ± 0.30	−20.54 ± 0.27	−21.00 ± 0.52	−21.25 ± 0.04	−21.38 ± 0.30	4.02	8.63
HIPEQ0107 + 01	8.5 ± 1.1	··· ···	7.7 ± 0.6	−13.83 ± 0.31	−14.68 ± 0.27	−14.95 ± 0.43	−15.10 ± 0.14	−15.13 ± 0.31	0.44	1.09
HIPEQ0119 + 00	62.1 ± 8.1	··· ···	8.6 ± 0.6	−16.10 ± 0.37	−16.91 ± 0.29	−17.24 ± 0.43	−17.37 ± 0.17	−17.50 ± 0.37	2.14	4.65
HIPEQ0120−00	24.0 ± 3.1	67.8 ± 13.3	8.7 ± 0.6	−16.20 ± 0.31	−16.99 ± 0.27	−17.31 ± 0.42	−17.46 ± 0.14	−17.54 ± 0.31	2.12	4.14
HIPEQ0122 + 00	33.0 ± 4.3	134.2 ± 12.9	9.9 ± 0.6	−20.42 ± 0.30	−20.89 ± 0.27	−20.98 ± 0.39	−21.10 ± 0.17	−21.14 ± 0.30	8.54	16.89

Notes. [a] Rotational velocities are derived from W_{20} values. Galaxies without proper inclination corrections have been omitted.

(This table is available in its entirety in machine-readable and Virtual Observatory (VO) forms in the online journal. A portion is shown here for guidance regarding its form and content.)

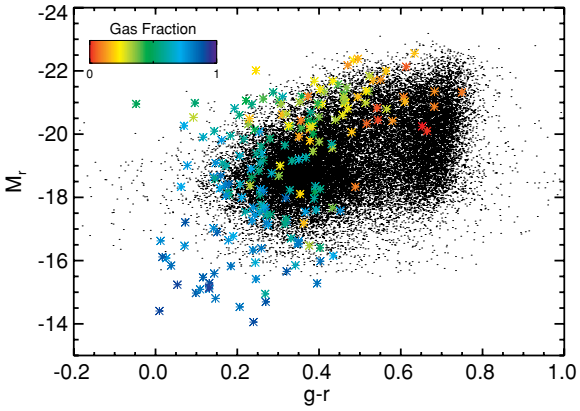

Figure 7. Absolute r-band magnitude as a function of $g - r$ for the H I-selected galaxies (color asterisks) and the SDSS DR4 main galaxy sample (black dots). ES/SDSS galaxies have been color coded according to their gas fractions. The H I-selection identifies a bluer and less luminous sample of galaxies than those used in typical SDSS studies.

(A color version of this figure is available in the online journal.)

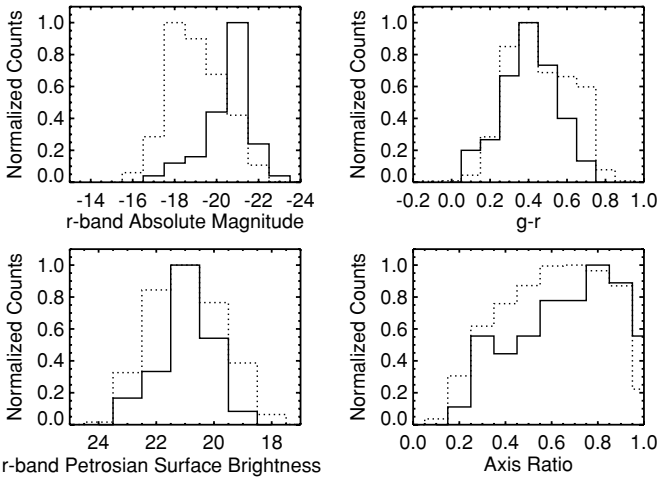

Figure 8. Normalized distributions of r-band absolute magnitude (top left), $g - r$ color (top right), r-band Petrosian surface brightness (bottom left) and axis ratio (bottom right) for the ES/SDSS (solid) and SDSS DR4 (dotted) galaxies that fall within the overlap region of the two samples (40 Mpc $< D <$ 140 Mpc). While the surface brightness distributions are similar, the ES/SDSS galaxies are bluer, intrinsically brighter and more likely to be face-on than the DR4 galaxies in the same volume.

on the spectral targeting (which does not select LSB galaxies), the photometric pipeline problems (which make nearby galaxies in SDSS difficult to analyze), and the fact that we sampled a very different volume than typical SDSS studies (see Figure 6). Despite, the heavy selection effects, it is important to demonstrate how an H I-selected sample produces a drastically different sample than a typical SDSS galaxy study. These differences can be seen in Figure 7, the M_r versus $g - r$ color–magnitude diagram for the H I-selected galaxies (color asterisks) and the DR4 SDSS main galaxy sample (black dots). All of the photometric corrections have been applied except for the internal extinction, which requires information about the rotation velocity (a quantity that is not available for the DR4 galaxies). The ES/SDSS data have been color coded according to their gas fractions.[13] While the bimodal distribution of DR4 galaxies can be clearly seen in Figure 7, the ES/SDSS sample dominates the blue distribution. The galaxies with the highest gas fractions occupy the bluest, lowest luminosity region of color–magnitude space. These trends between color, luminosity, and gas content are investigated in other studies (Garcia-Appadoo et al. 2009; West et al. 2009). Because of the way that SDSS galaxies are selected for both spectroscopy and scientific analysis, most SDSS studies do not include the bluest, faintest galaxies that are easily identified in an H I-selected sample.

To eliminate some of the selection effects due to sampling different volumes, we limited our comparison between the DR4 and ES/SDSS galaxies to those that fall within the overlap region of the two samples (40 Mpc $< D <$ 140 Mpc). There are 51 ES/SDSS and 18,379 DR4 galaxies in this volume. Figure 8 shows the normalized distributions for four measured or derived properties of the ES/SDSS (solid) and SDSS DR4 (dotted) galaxies. We calculated the mean values for each distribution as well as computed the Kolmogorov–Smirnov (KS) statistic to determine how likely the two histograms were drawn from the same distribution. The r-band Petrosian surface brightness distributions (bottom left) of the two populations are very similar, with both the ES/SDSS and DR4 samples having mean values of 20.9 mag arcsec^{-2} and a KS probability of 0.19 (19% chance of being pulled from the same distribution). The ES/SDSS galaxies are both bluer (average $g - r$ values of 0.40 versus 0.47; top right) and intrinsically brighter (M_r values of -20.6 versus -19.0; top left) than the DR4 SDSS main galaxies in the same volume. Both the properties have KS probabilities that give them a $< 3\%$ chance of the ES/SDSS and DR4 galaxies being pulled from the same distribution. Some of the discrepancy between the distributions is due to a significant population of dwarf elliptical galaxies in the DR4 sample that have high surface brightnesses (and thus are targeted for spectroscopy) and have small or non-existent quantities of gas (and are omitted from an H I-selected sample). In addition, the bluer $g - r$ colors in the ES/SDSS galaxies may be indicative of a recent burst of star formation in galaxies with a reservoir of gas (West et al. 2009).

The axis ratio distribution demonstrates a slight bias toward face-on galaxies in the ES/SDSS sample. The mean axis ratios are 0.67 and 0.61 for the ES/SDSS and DR4 samples, respectively. There is a 7% chance that the histograms are pulled from the same distribution. While the SDSS selection should be almost independent of axis ratio (and therefore be fairly representative of the population), H I-selected samples should have a slight bias toward face-on systems (the same amount of H I flux will be distributed into fewer channels in a face-on galaxy, resulting in brighter peak flux and easier detection). Figure 8 highlights an intrinsic bias in H I-selected surveys that will be important to consider for the next-generation H I surveys like ALFALFA (Giovanelli et al. 2005), which will include tens of thousands of H I-selected sources.

6. SUMMARY

Using our customized software for analyzing large galaxies in the SDSS, we have created an H I-selected catalog using data from the ES and SDSS surveys. The data are uniformly sampled and have well-characterized uncertainties and limitations. Our software addresses the deblending and sky subtraction issues that make SDSS catalog-level photometry of angularly large galaxies in SDSS unreliable. We specifically discussed the problems with deblending and sky subtraction and quantified their effect on the ES/SDSS sample. In addition, we derived a

[13] Gas fraction is defined as the mass in H I (corrected for heavier elements) divided by the sum of the mass in H I and stars ($f_{\rm gas} = 1.4{\rm M}_{\rm H\,I}/(1.4{\rm M}_{\rm H\,I} + {\rm M}_*)$).

hyperplane that relates the amount of flux removed by the sky subtraction algorithm to the size, magnitude, and axis ratio of the galaxy.

The ES/SDSS galaxies span a large range of surface brightnesses, colors, and stellar masses and as expected, the optical properties are different from those of most SDSS galaxy samples (mostly due to selection effects), as well as an optically selected sample compared at the sample volume. Specifically, the H I selection identifies galaxies with lower surface brightness, smaller absolute magnitudes, bluer colors, and smaller stellar masses than those used in typical SDSS studies.

H I-selected galaxies (compared to optically selected galaxies in the same volume) are bluer and brighter, the latter due to the abundance of dwarf elliptical galaxies in optically selected samples. The ES/SDSS sample also shows a slight bias toward face-on systems, a symptom of the H I selection.

Other papers incorporate the ES H I data and investigate how the SDSS photometric trends relate to the galaxy gas content (Garcia-Appadoo et al. 2009) and attempt to understand the colors of the galaxies (West et al. 2009). Future work will examine the dynamics of the ES/SDSS sample and investigate the Tully Fisher relation and its scatter.

The authors gratefully acknowledge the financial support of the Astronaut Scholarship Foundation, ADVANCE, ARCS, the Royalty Research Fund, NSF grant 0540567, the Theodore Jacobsen Fund. We also extend our gratitude to the anonymous referee who provided a substantial amount of feedback, which was extremely useful to the completion of this paper. A.A.W. thanks David Hogg, Mike Blanton, Marla Geha, Beth Willman, Anil Seth, Adam Burgasser, Kevin Covey, John Bochanski, and Maritza Tavarez-Brown for their helpful comments, suggestions, financial support, and gentle prodding.

Funding for the SDSS and SDSS-II has been provided by the Alfred P. Sloan Foundation, the Participating Institutions, the National Science Foundation, the U.S. Department of Energy, the National Aeronautics and Space Administration, the Japanese Monbukagakusho, the Max Planck Society, and the Higher Education Funding Council for England. The SDSS Web Site is http://www.sdss.org/.

The SDSS is managed by the Astrophysical Research Consortium for the Participating Institutions. The Participating Institutions are the American Museum of Natural History, Astrophysical Institute Potsdam, University of Basel, Cambridge University, Case Western Reserve University, University of Chicago, Drexel University, Fermilab, the Institute for Advanced Study, the Japan Participation Group, Johns Hopkins University, the Joint Institute for Nuclear Astrophysics, the Kavli Institute for Particle Astrophysics and Cosmology, the Korean Scientist Group, the Chinese Academy of Sciences (LAMOST), Los Alamos National Laboratory, the Max-Planck-Institute for Astronomy (MPIA), the Max-Planck-Institute for Astrophysics (MPA), New Mexico State University, Ohio State University, University of Pittsburgh, University of Portsmouth, Princeton University, the United States Naval Observatory, and the University of Washington.

REFERENCES

Abazajian, K., et al. 2004, AJ, 128, 502
Abazajian, K. N., et al. 2009, ApJS, 182, 543
Adelman-McCarthy, J. K., et al. 2006, ApJS, 162, 38
Adelman-McCarthy, J. K., et al. 2008, ApJS, 175, 297
Agüeros, M. A., et al. 2005, AJ, 130, 1022
Bailin, J., & Harris, W. E. 2008, ApJ, 681, 225
Barnes, D. G., et al. 2001, MNRAS, 322, 486
Begum, A., Chengalur, J. N., Karachentsev, I. D., Kaisin, S. S., & Sharina, M. E. 2006, MNRAS, 365, 1220
Bell, E. F., McIntosh, D. H., Katz, N., & Weinberg, M. D. 2003, ApJS, 149, 289
Bernardi, M. 2007, AJ, 133, 1954
Bertin, E., & Arnouts, S. 1996, A&AS, 117, 393
Blanton, M. R., Geha, M., & West, A. A. 2008, ApJ, 682, 861
Blanton, M. R., et al. 2001, AJ, 121, 2358
Blanton, M. R., et al. 2003a, AJ, 125, 2348
Blanton, M. R., et al. 2003b, ApJ, 594, 186
Burkholder, V., Impey, C., & Sprayberry, D. 2001, AJ, 122, 2318
Covey, K. R., et al. 2007, AJ, 134, 2398
Covey, K. R., et al. 2008, ApJS, 178, 339
Disney, M. J. 1976, Nature, 263, 573
Disney, M. J., Romano, J. D., Garcia-Appadoo, D. A., West, A. A., Dalcanton, J. J., & Cortese, L. 2008, Nature, 455, 1082
Doyle, M. T., et al. 2005, MNRAS, 361, 34
Fisher, J. R., & Tully, R. B. 1981, ApJS, 47, 139
Fukugita, M., Ichikawa, T., Gunn, J. E., Doi, M., Shimasaku, K., & Schneider, D. P. 1996, AJ, 111, 1748
Garcia-Appadoo, D. A., West, A. A., Dalcanton, J. J., Cortese, L., & Disney, M. J. 2009, MNRAS, 394, 340
Gavazzi, G., & Boselli, A. 1996, Astrophys. Lett. Commun., 35, 1
Geha, M., Blanton, M. R., Masjedi, M., & West, A. A. 2006, ApJ, 653, 240
Giovanelli, R., et al. 2005, AJ, 130, 2598
Gunn, J. E., et al. 1998, AJ, 116, 3040
Gunn, J. E., et al. 2006, AJ, 131, 2332
Hambly, N. C., Davenhall, A. C., Irwin, M. J., & MacGillivray, H. T. 2001a, MNRAS, 326, 1315
Hambly, N. C., Irwin, M. J., & MacGillivray, H. T. 2001b, MNRAS, 326, 1295
Hambly, N. C., et al. 2001c, MNRAS, 326, 1279
Haynes, M. P., Giovanelli, R., Chamaraux, P., da Costa, L. N., Freudling, W., Salzer, J. J., & Wegner, G. 1999, AJ, 117, 2039
Helmboldt, J. F., Walterbos, R. A. M., Bothun, G. D., O'Neil, K., & de Blok, W. J. G. 2004, ApJ, 613, 914
Henning, P. A. 1992, ApJS, 78, 365
Henning, P. A. 1995, ApJ, 450, 578
Hogg, D. W., Finkbeiner, D. P., Schlegel, D. J., & Gunn, J. E. 2001, AJ, 122, 2129
Iglesias-Páramo, J., et al. 2003, A&A, 406, 453
Ivezić, Ž., et al. 2004, Astron. Nachr., 325, 583
Jarrett, T. H., Chester, T., Cutri, R., Schneider, S., Skrutskie, M., & Huchra, J. P. 2000, AJ, 119, 2498
Karachentsev, I. D., Karachentseva, V. E., Huchtmeier, W. K., & Makarov, D. I. 2004, AJ, 127, 2031
Kennicutt, R. C., Tamblyn, P., & Congdon, C. E. 1994, ApJ, 435, 22
Lauer, T. R., et al. 2007, ApJ, 662, 808
Lupton, R. H., Gunn, J. E., & Szalay, A. S. 1999, AJ, 118, 1406
Lupton, R. H., Ivezic, Z., Gunn, J. E., Knapp, G., Strauss, M. A., & Yasuda, N. 2002, Proc. SPIE, 4836, 350
Mandelbaum, R., et al. 2005, MNRAS, 361, 1287
Masjedi, M., et al. 2006, ApJ, 644, 54
Matthews, L. D., Gallagher, J. S., & van Driel, W. 1999, AJ, 118, 2751
McGaugh, S. S., & de Blok, W. J. G. 1997, ApJ, 481, 689
Meyer, M. J., et al. 2004, MNRAS, 350, 1195
Obrić, M., et al. 2006, MNRAS, 370, 1677
Petrosian, V. 1976, ApJ, 209, L1
Pier, J. R., Munn, J. A., Hindsley, R. B., Hennessy, G. S., Kent, S. M., Lupton, R. H., & Ivezić, Ž. 2003, AJ, 125, 1559
Pizagno, J., et al. 2005, ApJ, 633, 844
Roberts, M. S. 1963, ARA&A, 1, 149
Rosenberg, J. L., & Schneider, S. E. 2000, ApJS, 130, 177
Rosenberg, J. L., & Schneider, S. E. 2002, ApJ, 567, 247
Rosenberg, J. L., Schneider, S. E., & Posson-Brown, J. 2005, AJ, 129, 1311
Sérsic, J. L. 1968, Bol. Asoc. Argentin. Astron. Plat. Argentin., 13, 20
Salim, S., et al. 2005, ApJ, 619, L39
Serra, P., Trager, S. C., van der Hulst, J. M., Oosterloo, T. A., Morganti, R., van Gorkom, J. H., & Sadler, E. M. 2007, New Astron. Rev., 51, 3
Schlegel, D. J., Finkbeiner, D. P., & Davis, M. 1998, ApJ, 500, 525
Scodeggio, M., & Gavazzi, G. 1993, ApJ, 409, 110
Smith, J. A., et al. 2002, AJ, 123, 2121
Smolčić, V., et al. 2006, MNRAS, 371, 121
Spitzak, J. G., & Schneider, S. E. 1998, ApJS, 119, 159
Staveley-Smith, L., et al. 1996, PASA, 13, 243
Stoughton, C., et al. 2002, AJ, 123, 485

Strauss, M. A., et al. 2002, AJ, 124, 1810
Swaters, R. A., van Albada, T. S., van der Hulst, J. M., & Sancisi, R. 2002, A&A, 390, 829
Terry, J. N., Paturel, G., & Ekholm, T. 2002, A&A, 393, 57
Theureau, G., Rauzy, S., Bottinelli, L., & Gouguenheim, L. 1998, A&A, 340, 21
Tucker, D. L., et al. 2006, Astron. Nachr., 327, 821
Tully, R. B., Pierce, M. J., Huang, J., Saunders, W., Verheijen, M. A. W., & Witchalls, P. L. 1998, AJ, 115, 2264
Walter, F., Brinks, E., de Blok, W. J. G., Bigiel, F., Kennicutt, R. C., Thornley, M. D., & Leroy, A. 2008, AJ, 136, 2563
West, A. A., Garcia-Appadoo, D. A., Dalcanton, J. J., Disney, M. J., Rockosi, C. M., & Ivezić, Ž. 2009, AJ, 138, 796
Wong, O. I., Webster, R., Kilborn, V., Waugh, M., & Staveley-Smith, L. 2009, MNRAS, 399, 2264
Wong, O. I., et al. 2006, MNRAS, 371, 1855
Yasuda, N., et al. 2001, AJ, 122, 1104
York, D. G., et al. 2000, AJ, 120, 1579
Zhang, W., Li, C., Kauffmann, G., Zou, H., Catinella, B., Shen, S., Guo, Q., & Chang, R. 2009, MNRAS, 397, 1243
Zwaan, M. A., Briggs, F. H., Sprayberry, D., & Sorar, E. 1997, ApJ, 490, 173
Zwaan, M. A., et al. 2004, MNRAS, 350, 1210